Fast, Accurate, and Precise Mapping of the RF Field In Vivo Using the 180° Signal Null

Nicholas G. Dowell* and Paul S. Tofts

RF field B_1 nonuniformity is the largest cause of error in the quantitative measurement of many clinically relevant parameters in MR images and spectra. Knowledge of the absolute flip angles at every region will improve the accuracy and precision of such parameters. This method uses the 180° signal null to construct a flip angle map of the entire brain in less than 4 min, independent of T_1, T_2, and proton density. Three spoiled gradient echo volume acquisitions of the whole brain were made with three different flip angles. The optimum choice of flip angles was determined to be 145°, 180°, and 215°. Linear regression analysis was used to determine the nominal (system calibrated) flip angle required for a signal null at every pixel and thence determine the absolute flip angle at that location. The experiment utilizes an existing MR sequence supplied by the scanner manufacturer. The technique is validated experimentally and a theoretical investigation into the optimum experimental parameters is presented. Magn Reson Med 58: 622–630, 2007. © 2007 Wiley-Liss, Inc.

Key words: RF mapping; inhomogeneity; in vivo; absolute flip angle

There are a growing number of MR parameters that give an insight into the physiological condition of the brain. The demand for a reliable measurement of these quantities in the diagnosis and prognosis of disease has placed increased importance on the accuracy and precision of quantitative MR (qMR) imaging techniques. Undoubtedly one of the most important factors affecting the accuracy and precision of many qMR parameters is B_1 field (or flip angle) inaccuracy. There are two distinct sources of these inaccuracies: first, errors in flip angle calibration during the prescan routine (which is designed to be correct for only the central portion of the prescribed volume) and second, the nonuniformity arising from the transmit coil and the conductivity, dielectric, and loading differences of the subject.

Quantitative measurements of proton density (PD), T_1, and magnetization transfer (MT) are all affected by inaccuracies in the calibration of the RF flip angle. These parameters are important markers for disease. For example, tissue water content is known to change with disease and this can be studied with MRI by measuring PD. Disease has also been shown to have a significant effect on tissue T_1 values and MT between protons in macromolecules, and free water can be a good marker for tissue damage. The problem of B_1 inhomogeneity worsens at higher B_0 (1) and, as the demand for high field MR systems grows, more emphasis will be placed on an accurate and precise quantification of the B_1 field. This is highlighted by the recent active research in this area (2–4).

The ideal approach for mapping the B_1 field would be accurate, precise, have a short scan time, and be independent of T_1 and slice (or slab) profile effects. Existing methods for B_1 mapping include taking the ratio of signal intensities (5–8), incrementing flip angles (9), using stimulated echoes in multipulse sequences (3,10,11), or by monitoring the signal phase (12,13). Each methodology above has its own advantages and drawbacks. Most methods study a change in signal intensity as a function of flip angle. With such an approach a common confound is that of T_1 dependence, where images may be T_1-weighted as a function of flip angle. This problem can be overcome by using a repetition time TR that is in excess of five times the longest T_1 in the sample, as in the double angle method (5). In the head, for example, the T_1 of cerebrospinal fluid (CSF) can be as long as 4 sec, thereby requiring a repetition time of 20 sec or longer. This can lead to very long overall acquisition times for multislice or 3D imaging, although several modifications have been proposed that shorten acquisition times (2,7).

Test objects, or phantoms, have been used to map the B_1 field. Although they have the advantage of ensuring a homogeneous sample over the volume of the coil, undergo no movement during the scan, and permit long acquisition times, they do not accurately reflect the spatial dependence of the RF field in vivo since their dielectric properties differ from those of the head (14,15).

Two-dimensional multislice acquisitions may suffer from slice profile distortions. Shaped excitation pulses are designed to give sharp-sided rectangular slice profiles when the RF pulse is applied at an optimum flip angle. However, when the pulse is required to yield a different flip angle, slice profile distortions are observed (16,17). Hence, integrating across the volume of a slice may introduce errors in the calculation of B_1. In addition, the 2D multislice method of determining B_1 may also suffer from in-flow effects between slices from mobile fluids such as blood and CSF, thus introducing further inaccuracies.

By implementing a 3D spoiled gradient echo (SPGR) experiment without a slab select gradient we avoid introducing slice profile and in-flow inaccuracies. The technique uses the 180° signal null (which is independent of T_1) to allow short TR to be used. It is envisaged that this technique will be incorporated into relevant qMR scanning protocols without significantly increasing total scan times. The method introduced here was inspired by the

NMR Research Unit, Institute of Neurology, University College London, London, UK.

Grant sponsor: Multiple Sclerosis Society of Great Britain and Northern Ireland.

Current address for P.S. Tofts: Brighton and Sussex Medical School, Brighton, BN1 9RR, UK.

*Correspondence to: Nicholas G. Dowell, NMR Research Unit, Institute of Neurology, University College London, London WC1N 3BG, UK. E-mail: n.g.dowell@ion.ucl.ac.uk

Received 27 July 2006; revised 27 October 2006; accepted 28 June 2007.

DOI 10.1002/mrm.21368

Published online in Wiley InterScience (www.interscience.wiley.com).

© 2007 Wiley-Liss, Inc.

work of Venkatesan et al. (18). However, we have adapted the method to yield a map of absolute flip angles over the entire brain in less than 4 min, without the need for a homogeneous phantom.

THEORY

The flip angle θ and RF field strength are related by:

$$\theta = \gamma B_1 \tau, \qquad [1]$$

where γ is the gyromagnetic ratio and τ is the RF pulse duration. However, in the presence of B_1 nonuniformity, there will be a discrepancy between the *nominal* (system-calibrated) flip angle θ_n and the *actual* (true) flip angle θ_a. Thus, θ_a at a position r is given by:

$$\theta_a(r) = \zeta(r)\theta_n, \qquad [2]$$

where the Greek letter zeta $\zeta(r)$ is the B_1 scaling factor at position r.

The transverse magnetization from an SPGR experiment is modeled (19) by the equation:

$$M_{xy} = M_0 \frac{1 - \exp\{-TR/T_1\}}{1 - \cos\theta_a \exp\{-TR/T_1\}} \sin\theta_a, \qquad [3]$$

where M_0 is the magnetization at thermal equilibrium. Transverse relaxation is not included in this equation because echo time and T_2 will only scale the signal amplitude and does not affect the signal null.

Figure 1 shows a plot of M_{xy} versus θ_a for the model in Eq. [3]. When $\theta_a \neq 180°$, the signal intensities are dependent on the ratio TR/T_1 and, consequently, it is impossible to determine ζ unless the T_1 is known. However, when $\theta_a = 180°$ the signal intensity is zero irrespective of T_1. Hence, at every location r the nominal flip angle that yields a signal null, $\theta_n^{null}(r)$, corresponds to $\theta_a(r) = 180°$. Thus, a flip angle scaling factor $\zeta(r)$ can be determined:

$$\zeta(r) = \frac{180°}{\theta_n^{null}(r)} \qquad [4]$$

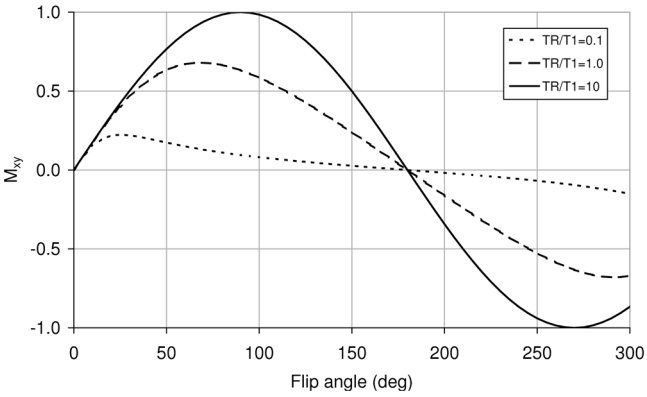

FIG. 1. Plot of simulated spoiled gradient echo transverse magnetization versus flip angle θ_a for a range of T_1.

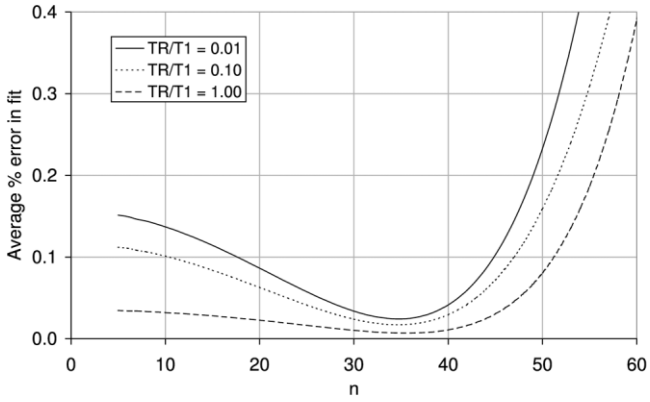

FIG. 2. The error introduced by using linear regression with three points at $\theta_n = 180° - n$, 180°, $180° + n$. The deviation from the model is expressed as an average over the range $0.85 \leq \zeta \leq 1.20$. The minimum error is found when $n = 35°$, i.e., $\theta_n = 145°$, 180°, 215°.

It should also be noted that M_{xy} varies approximately linearly with respect to the flip angle in the region where $\theta_a \approx 180°$. Therefore, by acquiring sets of images with different flip angles in this linear region, the corresponding signal intensities from position r may be fitted to a straight line to determine $\theta_n^{null}(r)$, and hence $\zeta(r)$, over all r in the presence of B_1 inhomogeneity.

A birdcage head coil affords good RF uniformity over the region of the brain and the flip angle scaling factor is likely to be within the range $0.85 < \zeta < 1.20$ (14). Within this range the data can be fitted to a straight line, although the accuracy may be improved by a judicious choice of flip angles. Since the shortest total acquisition time is desirable, we shall only consider the use of data from three measurements; i.e., a set of three flip angles $(180° - n)$, 180°, $(180° + n)$. Figure 2 shows the mean percentage error introduced into ζ by fitting the signal values from Eq. [3] to a straight line. The highest degree of accuracy is achieved when $n = 35$; i.e., using the set of flip angles 145°, 180°, 215°. The absolute percentage error introduced by the linear fit (using the optimum angles found above) is dependent on ζ and is less than 0.5% (Fig. 3). This is less

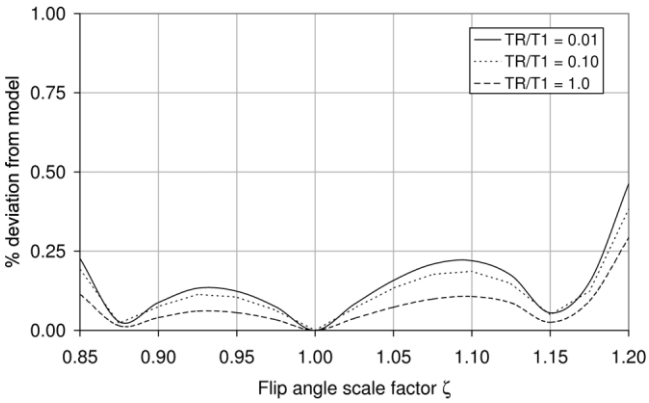

FIG. 3. The absolute (unsigned) percentage difference in ζ calculated with linear regression (using $\theta_n = 145°$, 180°, 215°) and the true value of ζ from the model expressed in Eq. [3].

than the typical variation due to scanner instability (20,21).

MATERIALS AND METHODS

All images were recorded on a General Electric 1.5T Signa Excite scanner (General Electric, Milwaukee, WI) with the 11X software version installed. The maximum gradient strength is 33 mTm^{-1} and a transmit-receive quadrature birdcage head coil was used. The flip angle maps were calculated from three image sets with θ_n = 145°, 180°, 215°. Each set was acquired using a 3D SPGR sequence with TR = 33 ms, echo time TE = 6 ms, and 28 slices, number of signal averages = 1, unless stated otherwise. The total acquisition time per image set is 70 sec. Further imaging parameters are included in the relevant sections below.

In conventional imaging the pulse flip angle for the SPGR experiment rarely exceeds 90°, but here higher flip angles are required. When the desired flip angle can no longer be achieved by increasing the pulse amplitude, the scanner lengthens the RF pulse. Variable pulse duration will be avoided if the largest required pulse duration is used for all flip angles in the range 145–215° and the desired flip angle is achieved only by the attenuation of the pulse amplitude. Here, the pulse duration was fixed at 5 ms, and the default sinc pulse shape was used, consisting of three lobes and with a bandwidth of 800 Hz.

To avoid loss of signal intensity toward the edges of the prescribed volume through slab-profile effects, the slab-select gradient was not applied during the RF pulse. As a consequence, frequency-encoding must be employed along the superior/inferior direction to avoid aliasing from the shoulders and upper body. The data were collected as magnitude images and, consequently, the measured magnitude signal S_m is larger than the true signal intensity S_a owing to a contribution from the noise (22,23):

$$S_m \approx \sqrt{S_a^2 + \sigma^2}, \quad [5]$$

where σ is the standard deviation of the random noise determined by placing a region of interest (ROI) in the background, being careful to avoid signal artifact. Equation [5] was used to yield images of S_a prior to fitting. In-house software was used to perform a linear regression analysis of intensity versus θ_n for each pixel in the volume to determine $\theta_n^{null}(r)$ and hence $\zeta(r)$ by using Eq. [4]. The quality of the linear fit may be monitored with the correlation coefficient R^2 from the linear regression analysis. In this study, R^2 was calculated for all the flip angle maps shown and remained high ($R^2 \geq 0.996$).

The sign of the magnitude signal intensity was deduced during the linear regression analysis. Signal intensity is assumed to vary linearly as a function of θ_n in the region of θ_n^{null} and the negative sign is allocated in an iterative fashion until the best linear fit is found. For example, for three points the magnitude signal intensity is allocated the signs (+, +, +) or (+, +, −) or (+, −, −). It should be noted that the remaining combination (−, −, −) yields identical ζ and R^2 values as (+, +, +). The sign may only be ambiguous when $\theta_n \approx \theta_n^{null}$. Here the signal intensity approaches zero (after noise correction) and the sign of the signal intensity does not significantly affect the regression analysis. Alternatively, the sign of the magnitude signal intensity may be determined from the complex images by monitoring the change in sign of the complex dataset. For comparison, a flip angle scale factor map was calculated using both methods of sign allocation. In regions of good signal-to-noise ratio (SNR) both methods resulted in identical sign allocation and, therefore, gave flip angle scale factors that were identical. In regions of poor SNR (<5), where the sign of the intensity near the null is ambiguous, the value of ζ differed by less than 3%. As a result, it was concluded that the use of magnitude images to determine the sign is no less accurate than using complex data where the signal intensity varies linearly as a function of θ_n. In addition, most scanners typically store only the magnitude images by default and, therefore, it was more convenient to allocate the sign of signal intensities using a linear fit of magnitude image intensity. It is this method that is used here. To avoid fitting pixels that lie outside the sample volume a noise threshold was assigned after a manual inspection of the source images.

Relevance to Lower Flip Angles

The flip angle scale factor maps are determined using high flip angles that are not typical for conventional scanning. To confirm that ζ determined at these higher flip angles is applicable to lower, more typical flip angles, we analyzed signal intensity for a range of flip angles that covers both the typical SPGR flip angles (≈30°) as well as the higher flip angles that are used in the novel method introduced here. A large oil phantom was used consisting of a bottle of sunflower oil (24 cm diameter × 35 cm high) as a homogeneous phantom. Oil was chosen for its low dielectric constant. This ensures that dielectric resonance (15) (which artificially increases the RF field strength toward the center of the phantom) is small. The field of view (FOV) was 48 × 24 cm with an acquisition matrix size 128 × 64 × 32, and slice thickness 0.9 cm. For analysis of signal intensity, a 3 × 3 cm region of interest was placed at the center of the phantom.

Spatial Homogeneity of the Head Coil

To determine the spatial homogeneity of the head coil, the oil phantom (described above) was used. The large dimensions of the phantom ensure that the resulting flip angle scale factor map describes the spatial homogeneity of the whole volume of the coil. The flip angle scale factor maps were recorded according to the procedure described above. The FOV was 48 × 24 cm with an acquisition matrix size 128 × 64 × 32, and slice thickness 0.9 cm.

Effect of Varying T_1 and TR

When θ_a = 180°, the signal intensity of a sample will be nulled irrespective of the T_1 value (Eq. [3]). To confirm that this is the case, three test tubes (diameter 2 cm; length 8 cm) containing Eurospin agarose gels (Diagnostic Sonar, Livingstone, UK) (24,25) with T_1 values 329, 659, 1547 ms were scanned and the signal intensity was plotted as a function of θ_n. The gels were placed in a loading ring and

were scanned individually and in an identical location in the coil to exclude spatial B_1 variations. The images were acquired using the parameters noted above with matrix size 128 × 64 × 32, FOV 36 × 18 cm, and slice thickness 0.5 cm. Analysis of the signal intensity was made by placing an ROI in the central slice through the test tube.

The flip angle scale maps should also be independent of TR. Flip angle scale maps were recorded with TR = 16, 25, 33, 50, 100, 150 ms using ≈4 cm^3 of oil (T_1 ≈200 ms) in a test tube (2 cm diameter) located at the center of the coil and inside a loading ring. A small phantom size was used to minimize the variation in ζ due to spatial RF field inhomogeneity. Analysis was conducted using an ROI (0.8 cm × 0.8 cm) at the center of the oil. The matrix size was 128 × 64 × 32 with FOV 16 × 8 cm, slice thickness 0.6 cm.

Experimental Validation Using an Oil Phantom

To confirm that the proposed method can accurately determine ζ in an inhomogeneous RF field, the RF transmitter output voltage was manually adjusted through a series of power output values within the range +31.8 and −24.1% from the system-calibrated (prescan) value. A control scan using the prescan transmitter output voltage was also acquired. The experimentally determined value of ζ was compared to the expected value of ζ. The flip angle scale factor maps were collected using the small oil phantom described above. An ROI (0.8 cm × 0.8 cm) at the center of the oil was chosen for the analysis. Further imaging parameters: matrix size 128 × 96 × 32 with FOV 16 × 8 cm, slice thickness 0.6 cm.

Off-Resonance Effects

RF pulses act with maximum efficiency on spins that possess a resonant frequency close to that of the RF irradiation. The pulse is less effective for spins with an offset from resonance ($\Delta\nu$) and in such cases it may not be possible to effect a 180° null with a single pulse since magnetization will precess about an effective B_1 field that is tilted out of the transverse plane (26). In the head at B_0 = 1.5T the difference in magnetic susceptibility at the tissue–bone interface is typically in the region of $\Delta\nu$ = 15 Hz and in these regions the effect on ζ is negligible. However, in the areas of the frontal lobe adjacent to the air-filled sinuses, larger frequency offsets of $\Delta\nu$ = 100 – 200 Hz (27) are observed and, as a result, should be taken into account when calculating ζ using this method.

Off-resonance effects were explored by measuring the mean signal intensity (in an ROI located at the center of the coil) as a function of θ_n, with the transmitter frequency on resonance (as determined by the prescan calibration procedure) and off resonance by $\Delta\nu$ = 50, 100, 150 Hz. The sample was the large oil phantom described above. The matrix size was 128 × 64 × 32 with an FOV 48 × 24 cm and a slice thickness of 0.9 cm.

Flip Angle Scale Factor Map of a Water Phantom

In contrast to oil, water has a high dielectric constant and, consequently, the center of a spherical water phantom receives a higher RF field than the periphery (14,15). This results in a larger variation in ζ than would be observed with an oil phantom (although ζ remains within the range 0.85–1.20). The flip angle map was acquired of a 15-cm diameter sphere filled with water doped with nickel(II)sulfate placed inside a loading ring. Further imaging parameters: matrix size 128 × 64 × 32 with FOV 44 × 22 cm, slice thickness 0.5 cm.

In Vivo Flip Angle Scale Factor Map

The subject was a 28-year-old male. Informed consent was given by the subject and ethical approval for the study was obtained from the Joint Research Ethics Committee of the Institute of Neurology and the National Hospital for Neurology and Neuroscience. The matrix size was 128 × 64 × 32 with FOV 44 × 22 cm and slice thickness 0.5 cm.

RESULTS

Relevance to Lower Flip Angles

The dependence of the SPGR signal intensity on flip angle is closely modeled by Eq. [3] both in the high flip angle regime, where ζ is determined, and in the lower (more typical) flip angle regime (Fig. 4). The model fitting yielded ζ = 1.175 using all the points in the curve and the linear fitting using only three points near the null (150°, 180°, 210°) yielded ζ = 1.177. This close agreement indicates that ζ found using the linear fitting method is valid for all flip angles over this range.

Spatial Homogeneity of the Head Coil

Figure 5 shows the sagittal central slice of the large oil phantom, recorded with flip angles near 180°. The head coil is approximately uniform at the center, and gives a low signal intensity at θ_n = 180° in this region. In contrast, the peripheral region of the phantom has higher signal intensity because a substantial portion of the oil extends beyond the central region of the coil, resulting in a lower RF field strength (and hence smaller θ_a). This is shown in the flip angle scale factor map in Fig. 5, which exhibits a smooth decrease in ζ as a function of distance from the

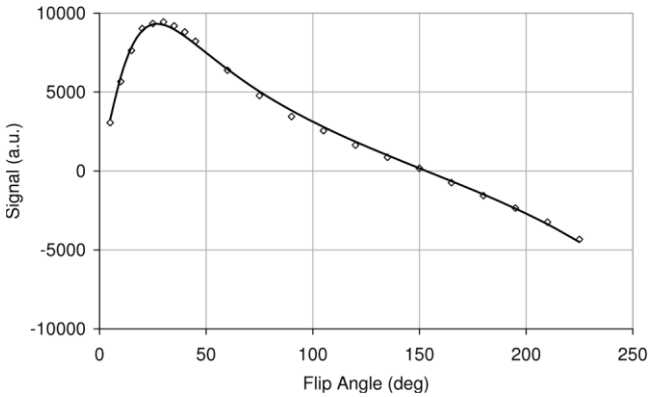

FIG. 4. Plot showing the flip-angle dependence of mean signal intensity in the central slice of a small (≈4 cm^3) oil phantom (open diamonds) with TR/T_1 = 0.165, using a sinc excitation pulse. The solid line represents the model fitting given by Eq. [3].

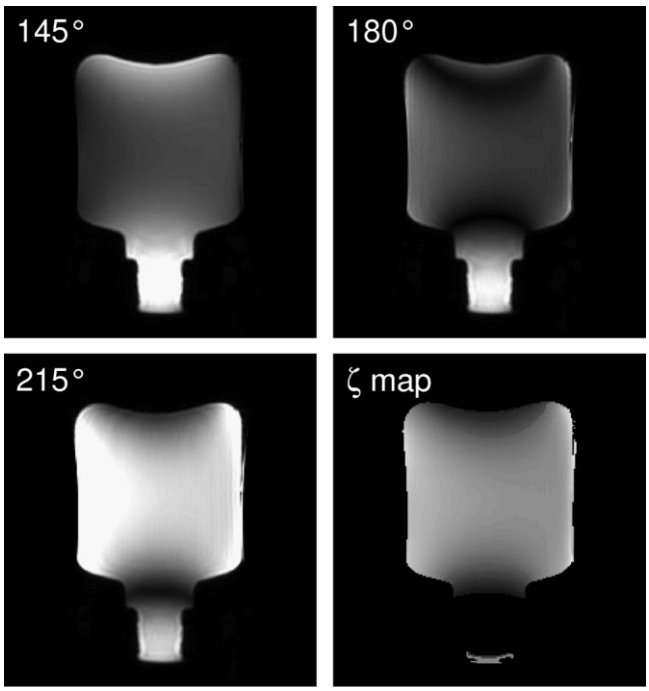

FIG. 5. The central slice of a large oil phantom (15 L) acquired with θ_n = 145°, 180°, and 215° and the resulting flip angle scale factor map, calculated from a pixel-by-pixel linear fitting of these images.

center of the coil. Also, there is an increase in ζ at the periphery of the phantom, where the oil is closest to the elements of the birdcage coil.

Effect of Varying T_1 and TR

Figure 6 shows the signal intensity of agarose Eurospin gels with known T_1 values. There is only a 1% variation in the value of θ_n^{null} determined for each gel, in spite of the differences in T_1 values. However, when $\theta_n \neq \theta_n^{null}$ the signal intensities become T_1-dependent.

The flip angle maps of the small oil phantom using a range of TR yielded the ζ values shown in Table 1. All values lie within the 95% confidence limit (±0.01), although there is a slight trend toward lower ζ as TR/T_1 decreases. At the lowest TR/T_1, a 2% difference in ζ is observed compared with the value determined at long TR. This loss of accuracy is due to the poor SNR that is observed as a result of scanning both with flip angles near the null and using a very short TR.

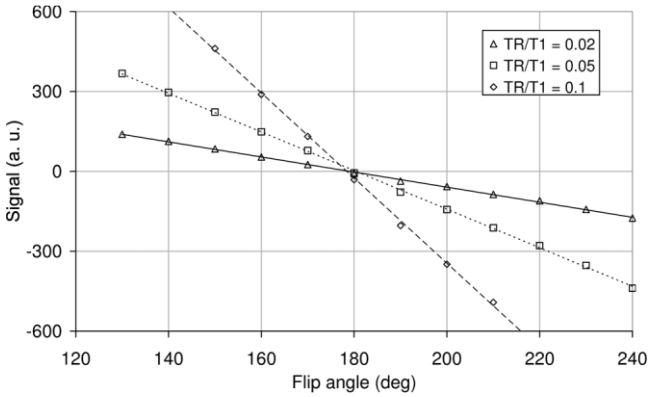

FIG. 6. Plot of signal intensity versus θ_n for three agarose gels with known T_1 values. Signal intensity has no T_1 dependence when θ_a = 180° although, as predicted, the signal intensity is T_1-dependent when $\theta_a \neq$ 180°. The TR was 33 ms.

Table 1
Experimental Dependence of Flip Angle Scaling Factor ζ on TR/T_1

TR/T_1	Mean ζ (measured)[a]
0.75	1.031
0.50	1.028
0.25	1.028
0.17	1.033
0.13	1.024
0.08	1.013

The phantom was a small volume of sunflower oil (~4 cm^3, $T_1 \approx$ 200 ms).
[a]95% confidence interval = ±0.01. Calculated as $\pm 1.96 \times SD/\sqrt{N}$ where SD is the standard deviation and N is the number of pixels in the ROI.

Experimental Validation Using an Oil Phantom

The experimental and theoretical values for a known change in transmitter output voltage are shown in Table 2. The experimentally determined values of ζ agree very closely with the theoretical scaling factor and lie well within the 95% confidence interval over the range $0.85 < \zeta < 1.20$. An underestimation of the flip angle scale factor is observed at the higher end of this range ($\zeta > 1.20$), whereas at the lower end of the range the deviation from the model is much smaller. A similar trend is exhibited by the expected percentage deviation from the model, shown in Fig. 3.

Table 2
Comparison of Theoretical and Experimental Flip Angle Scaling Factor ζ Calculated from a Small Volume of Sunflower Oil following Changes in the Transmitter Output

Change in transmitter output[a] %	Mean ζ (measured)[b]	Mean ζ (expected)[c]
−24.1	0.783	0.784
−18.7	0.840	0.840
−12.9	0.898	0.900
−6.7	0.963	0.964
Unchanged	1.033	1.033
+7.2	1.105	1.107
+14.8	1.181	1.186
+23.0	1.246	1.271
+31.8	1.296	1.362

[a]These measurements were recorded on a GE scanner where transmitter output voltage ∝ $10^{TG/200}$. Each successive increase in transmitter output corresponds to a change in transmitter gain TG = 6 units.
[b]95% confidence interval = ±0.01. Calculated as $\pm 1.96 \times SD/\sqrt{N}$ where SD is the standard deviation and N is the number of pixels in the ROI.
[c]Expected values calculated relative to the measured unchanged transmitter output, i.e., percent change in transmitter output × 1.033.

Off-Resonance Effects

Figure 7a shows a plot of the mean magnitude signal intensity in an ROI versus θ_n with several resonance offsets. The sign of the magnitude intensity was deduced by performing a least-squares fitting to the data, as described above. For the condition where $\Delta\nu = 0$ Hz (on resonance) a signal null occurs at $\theta_n = 159°$ yielding $\zeta = 1.133$. However, when the RF pulses were applied with $\Delta\nu \neq 0$ a signal null can no longer be achieved due to the presence of residual transverse magnetization (26). The largest deviation from the on-resonance case occurs when $\theta_n = \theta_n^{null}$, whereas further from the null point the signal intensity from the off-resonance data matches the on-resonance data more closely. Figure 7b shows the deviation in $\zeta(\Delta\nu)$ from $\zeta(\Delta\nu = 0)$ as a function of offset from resonance using the data in Fig. 7a. ζ is calculated by sampling the signal intensity at three points along the curve. Three conditions are considered: set 1 ($\theta_n = 140°, 180°, 220°$) represents the best case since the data are sampled such that θ_n^{null} (which equals 160° here) lies between the chosen points. Set 2 ($\theta_n = 130°, 170°, 210°$) represents sampling data closer to θ_n^{null}, and Set 3 ($\theta_n = 120°, 160°, 200°$) represents the worst case since the data is sampled at θ_n^{null}.

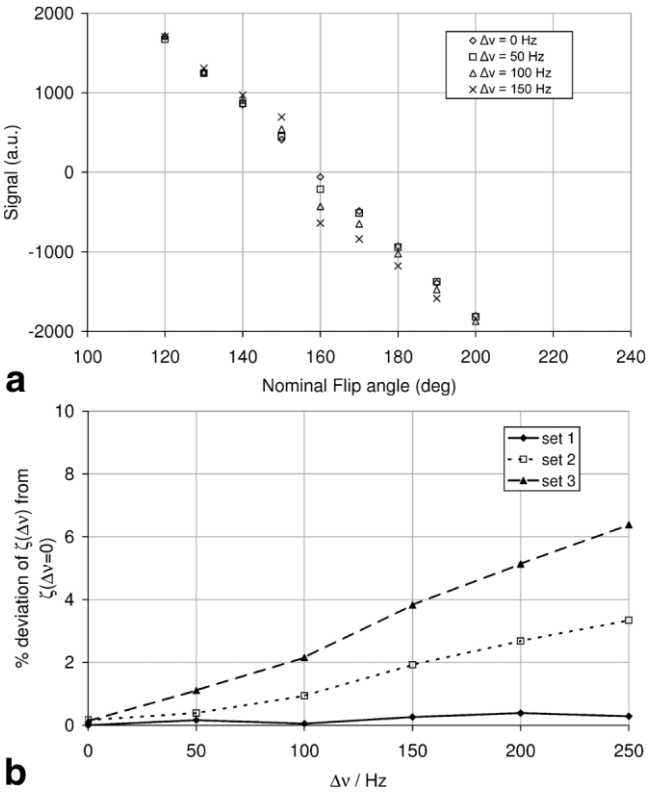

FIG. 7. (**a**) Signed magnitude signal intensity as a function of nominal flip angle for on-resonance and off-resonance conditions. Only minor deviation of signal intensity from the on-resonance condition is observed when $\theta_n \neq \theta_n^{null}$ at resonance offsets $\Delta\nu < 150$ Hz. (**b**) Absolute (unsigned) percentage deviation in ζ from on-resonance condition for three sets of nominal flip angles (see text). Signal intensity measurements were made from an ROI at the center of a large oil phantom.

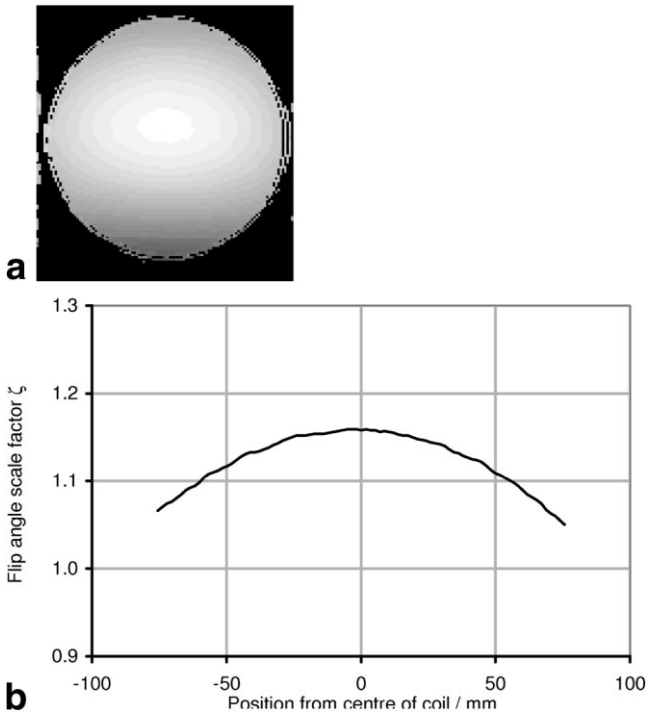

FIG. 8. (**a**) Axial slice from a flip angle scale factor map of a 15 cm diameter spherical water phantom and (**b**) the corresponding profile extracted along the right/left direction through the center of (**a**).

Flip Angle Scale Factor Map of a Water Phantom

The flip angle map of the water phantom shows high nonuniformity, as expected (Fig. 8a). The increase in ζ at the center of the phantom is a result of dielectric resonance and is clearly shown by the profile (Fig. 8b) taken through the center of the flip angle map.

In Vivo Flip Angle Scale Factor Map

Figure 9a–c shows three orthogonal projections through the brain, together with the corresponding flip angle maps (Fig. 9d–f). The flip angle maps are smooth over the region of the brain including the ventricles. The profiles through the flip angle map of the brain (Fig. 9g) shows a slight increase in RF field strength toward the center of the head (again due to dielectric resonance). This variation in B_1 across the head is well known and compares favorably with previous investigations (2,14) and, therefore, qualitatively validates this new approach. The correlation coefficient R^2 of the analysis showed that there is a good fit from all areas of the brain ($R^2 > 0.996$) even from regions that yield low signal intensity, such as the ventricles.

DISCUSSION AND CONCLUSIONS

The technique introduced here operates near the signal null and hence possesses relatively low signal intensity. However, the precision of this method is dependent on the *change* in signal with respect to flip angle. Since the signal changes rapidly in the neighborhood of the null (Fig. 1) a high degree of precision is obtained. Furthermore, the SNR may be improved by smoothing the images prior to anal-

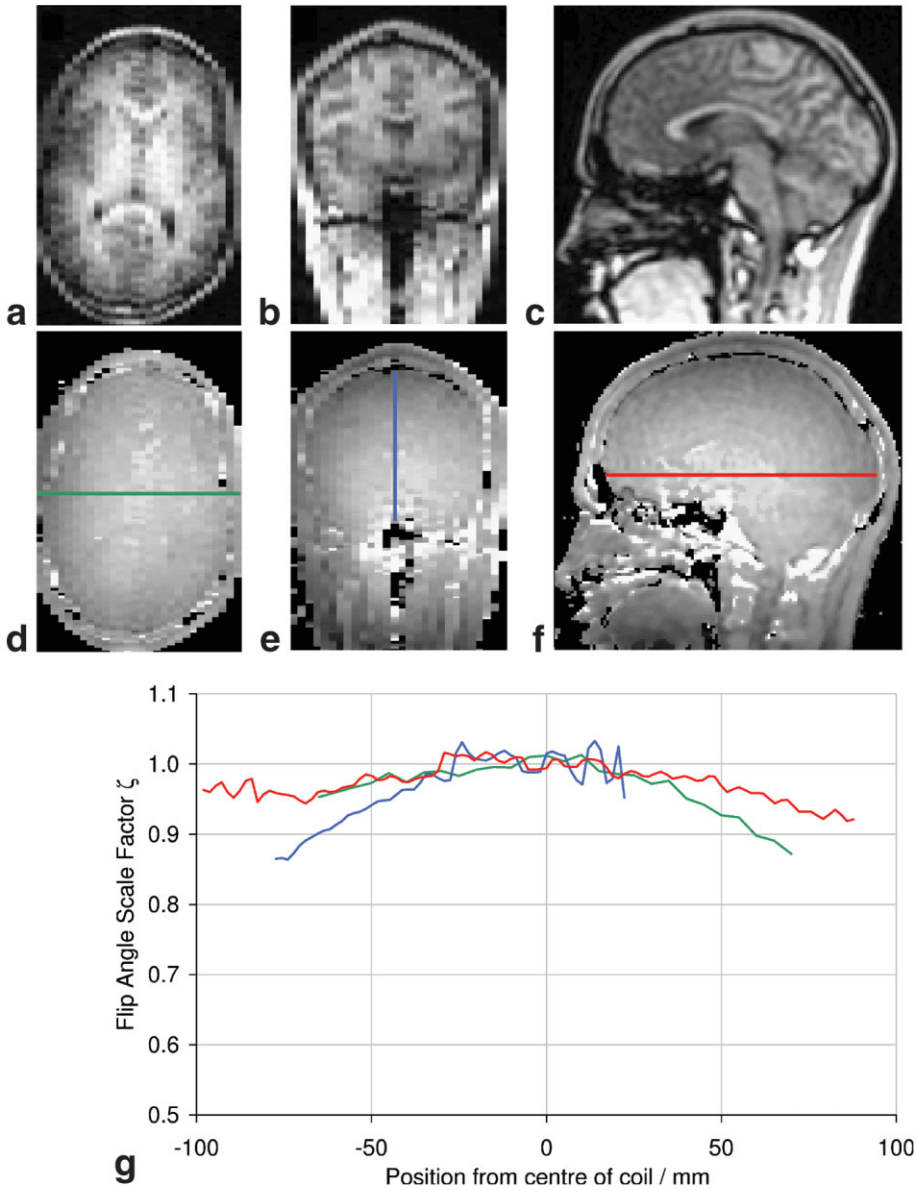

FIG. 9. (**a**) Axial-, (**b**) coronal-, and (**c**) sagittal-plane images of the brain (θ_n = 145°) and (**d–f**) the corresponding flip angle scale factor maps, shown without image smoothing. The profiles in (**g**) are extracted through the brain along the right/left (green), superior/inferior (blue), and anterior/posterior directions as indicated by the colored lines in (**d–f**).

ysis. The flip angle maps suffer no significant loss of resolution during this process owing to the smooth spatial variation in B_1.

Accurate quantitative MR studies in the head are particularly desirable and, as such, this linear fitting technique is well suited for use with head coils and body coils that provide a relatively homogeneous B_1 field. At higher B_0 field strengths or with typically nonhomogeneous hardware (such as transmission surface coils) it is possible that $\zeta < 0.85$ or $\zeta > 1.20$ and the signal intensity will no longer vary linearly as a function of flip angle in the neighborhood of $\theta_n = 180°$. Consequently, more than three values of θ_n, covering a wider flip angle range, may be required to ensure complete coverage of the θ_n^{null} region. Alternatively, a nonlinear approach (based on the model in Eq. [3]), could be employed to accurately determine θ_n^{null} and hence ζ.

The total acquisition time of this technique may be reduced by shortening TR. However, it should be remembered that the spins will be more saturated at shorter TR, and hence yield lower overall SNR. This may lead to reduced accuracy in ζ in regions of the brain that have long T_1 such as CSF in the ventricles. In addition, specific absorption rate (SAR) limits should be taken into account when implementing sequences that include high flip angle pulses, and longer TR should be used when SAR exceeds the recommended levels. We have found that TR = 33 ms is a suitable compromise yielding sufficient SNR and acceptable SAR levels in vivo at 1.5T. The RF field varies smoothly over the volume of the coil and only modest spatial resolution is required to describe the B_1 field. Therefore, the overall acquisition time could be shortened further by performing fewer phase-encoding steps and, additionally, the increased voxel size will benefit SNR. The SPGR sequence used in this study acquires a minimum of 64 phase-encoding lines, although a simple modification to the pulse sequence code would remove this limitation.

In the past, transmitter linearity across a wide range of flip angles was questionable. However, modern scanners

are able to produce linear increments in amplitude. The experimental validation shown in Table 2 indicates that the RF amplifier was able to achieve the expected changes in transmitter amplitude in this high-flip-angle regime. Although the RF pulses used in this experiment are designed for low-angle excitation, the absence of a slab-select gradient ensures that slab profile problems are avoided. This technique is based on the standard SPGR experiment and, therefore, the default sinc shape was chosen as the excitation pulse (16), although, in practice, other pulse shapes may be used to determine the ζ map.

An off-resonance pulse can be described by an effective field B_1^{eff} that is the resultant of the applied B_1 field and the residual B_0 field in the rotating frame. Consequently, B_1^{eff} is tilted out of the transverse plane and the magnetization precesses about a cone such that complete inversion is not possible. For the shaped sinc pulse, the B_1 field and hence the tilt angle for B_1^{eff} is time-varying but will remain either always above or always below the transverse plane. The larger the resonance offset the more B_1^{eff} is tilted out of the transverse plane causing the magnetization to precess about a narrower cone (26). At modest frequency offsets, such as those observed in the brain, the amount of transverse magnetization generated by an off-resonance pulse (where $\Delta\nu < 50$ Hz) is similar to that produced when $\Delta\nu = 0$. However, at the tissue–air boundary the resonant frequency is known to vary by up to ≈3 ppm ($\Delta\nu =$ 200 Hz at 1.5T) (27) and in such regions the set of flip angles that are chosen to sample the signal intensity becomes important. Figure 7b shows that when $\Delta\nu <$ 50 Hz the deviation in ζ is less than 1% even when sampling at θ_n^{null}. In addition, if data are sampled using Set 1 (avoiding θ_n^{null}), the deviation in ζ is less than 0.5% for large offsets up to $\Delta\nu = 150$ Hz. Therefore, if a high degree of accuracy is required in the regions of the brain where $\Delta\nu > 50$ Hz the signal intensity should not be sampled at θ_n^{null}. When this method is implemented for the first time, a more thorough, one-off investigation of the signal null should be made. For example, this may involve acquiring data from five flip angles to determine the value of θ_n^{null} more accurately. In Fig. 7 the calculated ζ parameter differs from the on-resonance condition by greater than 1% when $R^2 < 0.995$. We recommend that this threshold value of R^2 be used to identify potential areas of nonlinearity for which an alternate set of nominal flip angles should be considered.

Although a similar methodology was employed by Venkatesan et al. (18) to determine the flip angle scale factor for a single pixel, our approach uses the signal null to determine a flip angle map of entire volumes in vivo. As a consequence we have removed the necessity for a homogeneous phantom to determine flip angle maps. Furthermore, it has been possible to determine θ_n^{null} with fewer volume acquisitions due to a theoretical investigation into the optimum set of flip angles required for the linear fit. As a consequence, the total acquisition time has been reduced.

The method introduced here determines accurate flip angle maps of the entire brain in less than 4 min and can yield accuracy in ζ of better than 1% when the data points are sampled in a region where signal intensity varies linearly with flip angle. The technique uses an existing SPGR sequence that is available on all commercial scanners and may be widely implemented. The postprocessing is simple (based on linear regression) and requires only modest computer power. This technique can accurately determine absolute flip angles in the presence of T_1 weighting and, therefore, permits rapid acquisition using optimized scanning parameters that balance SAR, sensitivity, and speed.

ACKNOWLEDGMENTS

N.G.D. thanks Mara Cercignani, Dan J. Tozer, Jon S. Jackson, and Mark R. Symms for their help and advice.

REFERENCES

1. Collins CM, Yang QX, Wang JH, Zhang X, Liu H, Michaeli S, Zhu XH, Adriany G, Vaughan JT, Anderson P, Merkle H, Ugurbil K, Smith MB, Chen W. Different excitation and reception distributions with a single-loop transmit-receive surface coil near a head-sized spherical phantom at 300 MHz. Magn Reson Med 2002;47:1026–1028.
2. Cunningham CH, Pauly JM, Nayak KS. Saturated double-angle method for rapid B1+ mapping. Magn Reson Med 2006;55:1326–1333.
3. Jiru F, Klose U. Fast 3D radiofrequency field mapping using echo-planar imaging. Magn Reson Med 2006;56:1375–1379.
4. Yarnykh VL. Actual flip-angle imaging in the pulsed steady state: a method for rapid three-dimensional mapping of the transmitted radiofrequency field. Magn Reson Med 2007;57:192–200.
5. Stollberger R, Wach P, McKinnon G, Justich E, Ebner F. RF-field mapping in vivo. In: Proceedings of the SMRM, 7th Annual Meeting, San Francisco, CA, 1988. p 106.
6. Insko EK, Bolinger L. Mapping of the radiofrequency field. J Magn Reson A 1993;103:82–85.
7. Stollberger R, Wach P. Imaging of the active B_1 field in vivo. Magn Reson Med 1996;35:246–251.
8. Samson RS, Wheeler-Kingshott CAM, Symms MR, Tozer DJ, Tofts PS. A simple correction for B-1 field errors in magnetization transfer ratio measurements. Magn Reson Imaging 2006;24:255–263.
9. Hornak JP, Szumowski J, Bryant RG. Magnetic-field mapping. Magn Reson Med 1988;6:158–163.
10. Carlson JW, Kramer DM. Rapid radiofrequency calibration in MRI. Magn Reson Med 1990;15:438–445.
11. Akoka S, Franconi F, Seguin F, Lepape A. Radiofrequency map of an NMR coil by imaging. Magn Reson Imaging 1993;11:437–441.
12. Oh CH, Hilal SK, Cho ZH, Mun IK. Radio-frequency field intensity mapping using a composite spin-echo sequence. Magn Reson Imaging 1990;8:21–25.
13. Bosak E, Schiff J, Kaplan N. Radiofrequency power calibration for magnetic resonance imaging using signal phase as indicator. Magn Reson Med 1999;41:474–478.
14. Barker GJ, Simmons A, Arridge SR, Tofts PS. A simple method for investigating the effects of non-uniformity of radiofrequency transmission and radiofrequency reception in MRI. Br J Radiol 1998;71:59–67.
15. Tofts PS. Standing waves in uniform water phantoms. J Magn Reson B 1994;104:143–147.
16. Wang JH, Mao WH, Qiu ML, Smith MB, Constable RT. Factors influencing flip angle mapping in MRI: RF pulse shape, slice-select gradients, off-resonance excitation, and B-0 inhomogeneities. Magn Reson Med 2006;56:463–468.
17. Parker GJM, Barker GJ, Tofts PS. Accurate multislice gradient echo T-1 measurement in the presence of non-ideal RF pulse shape and RF field nonuniformity. Magn Reson Med 2001;45:838–845.
18. Venkatesan R, Lin WL, Haacke EM. Accurate determination of spin-density and T-1 in the presence of RF-field inhomogeneities and flip-angle miscalibration. Magn Reson Med 1998;40:592–602.

19. Tofts PS. The measurement process. In: Tofts PS, editor. Quantitative MRI of the brain. Chichester, UK: John Wiley & Sons; 2003. p 17–54.
20. Jackson JS, Tozer DJ, Tofts PS. Rapid measurement of subtle sub-one-percent changes in transmitter output and receive gain to monitor scanner stability. In: Proceedings of the ISMRM, 14th Annual Meeting, Seattle, WA, 2006. p 2363.
21. Weisskoff RM. Simple measurement of scanner stability for functional NMR imaging of activation in the brain. Magn Reson Med 1996;36:643–645.
22. Edelstein WA, Bottomley PA, Pfeifer LM. A signal-to-noise calibration procedure for NMR imaging-systems. Med Phys 1984;11:180–185.
23. Henkelman RM. Measurement of signal intensities in the presence of noise in MR images. Med Phys 1985;12:232–233.
24. Lerski RA. Trial of modifications to Eurospin MRI test objects. Magn Reson Imaging 1993;11:835–839.
25. Lerski RA, Decertaines JD. Performance assessment and quality-control in MRI by Eurospin test objects and protocols. Magn Reson Imaging 1993;11:817–833.
26. Ernst RR, Bodenhausen G, Wokaun A. Off-resonance effects due to finite pulse amplitude. In: Principles of nuclear magnetic resonance in one and two dimensions. Oxford: Clarendon Press; 1997. p 119–124.
27. Ericsson A, Weis J, Hemmingsson A, Wikstrom M, Sperber GO. Measurements of magnetic-field variations in the human brain using A 3D-FT multiple gradient-echo technique. Magn Reson Med 1995;33:171–177.